Microstructure and mechanical property evolution of friction stir welded (B₄C+Al₂O₃)/Al composites designed for neutron absorbing materials

ZAN YuNing[1,3], WANG BeiBei[1], ZHOU YangTao[1], JIA CunLei[1,3], LIU ZhenYu[1], WANG QuanZhao[2*], XIAO BoLv[1] & MA ZongYi[1*]

[1] *Shenyang National Laboratory for Materials Science, Institute of Metal Research, Chinese Academy of Sciences, Shenyang 110016, China;*
[2] *Key Laboratory of Nuclear Materials and Safety Assessment, Institute of Metal Research, Chinese Academy of Sciences, Shenyang 110016, China;*
[3] *School of Materials Science and Engineering, University of Science and Technology of China, Shenyang 110016, China*

(B₄C+Al₂O₃)/Al composite designed for the dry storage of spent nuclear fuels was fabricated and then subjected to friction stir welding, at a welding speed of 100 mm/min and rotation rates of 400–800 r/min. Sound joints were obtained under all welding parameters; however, significant softening occurred in the nugget zone (NZ) for all the joints. Therefore, all the joints exhibited significantly decreased strength at both room temperature and high temperature compared with the base metal, with the joints fracturing in the NZs. Rotation rate exhibited no obvious effect on the tensile strength of the joints, but led to increased elongation as the result of the broadened NZs. The detailed microstructural examinations indicated that the welding thermo-mechanical effect broke up the near 3D amorphous Al₂O₃ netlike structure distributed at the Al grain boundaries, caused the coarsening of Al grains, and the agglomeration and crystallization of amorphous Al₂O₃, thereby resulting in the softening of the NZs and the reduction in the joint strength. Consequently, inhibiting the breakup and crystallization of 3D amorphous Al₂O₃ netlike structure is the key factor to improve the joint strength of the (B₄C+Al₂O₃)/Al composite.

particle reinforced Al matrix composites, neutron absorber materials, FSW, mechanical properties, high-temperature strength

1 Introduction

Spent nuclear fuel, which refers to nuclear fuel that has been irradiated in a reactor, still has high radioactivity [1,2]. In order to avoid nuclear accidents caused by spallation neutrons, neutron absorber materials (NAMs) are necessary in the storage and transportation of spent nuclear fuels [2–4].

Boron carbide (B₄C) is often used in NAMs because of the neutron absorption ability of ¹⁰B [5]. However, since B₄C

ceramic is hard to deform, it is usually used as reinforcements in the composites [5,6]. B₄C reinforced Al matrix (B₄C/Al) composites possess high specific modulus, high specific strength, and high thermal stability, so they emerged as a kind of outstanding NAMs and are increasingly used in the storage and transportation of spent fuels [1,5].

In the traditional wet storage of the spent fuels, B₄C/Al NAMs (such as B₄C/6061Al composites) were used as functional materials together with other structural materials. In recent years, the dry storage of the spent fuels has been increasingly used, which put higher requests forward the

---

lightweight and heat-sinking capability. B_4C/Al NAMs are expected to satisfy both structural and functional demands. Therefore, studying the fabrication and application of the new generation of B_4C/Al NAMs with excellent high-temperature mechanical properties is of great significance.

A new kind of $(B_4C+Al_2O_3)$/Al NAM was recently developed for the dry-storage of the spent fuels in our laboratory. High-temperature strength of the composite was enhanced by amorphous Al_2O_3 (am-Al_2O_3) on the surface of ultrafine Al powders. The composite was proven to meet the strength requirement of independent load-carrying. However, the feasibility of its application is grounded in good weldability in the practical service.

Although particle reinforced aluminium matrix composites (PRAMCs) have been already used in aerospace and automotive industries [7], their application is usually constrained by the poor weldability [8]. It was hard for using traditional fusion or diffusion welding methods to achieve perfect welding. For instance, in study of TIG arc-welding of PRAMCs [8], it was reported that severe material degradation was produced because of the interfacial reaction between particles and molten Al matrix, porosity and particle aggregation. Diffusion welding of PRAMCs was also proven to be defective because of the huge difference between the ceramic particles and the matrix alloy [9].

Among various welding techniques, friction stir welding (FSW) was considered to be a promising method for welding the PRAMCs [10,11]. As a solid-state joining technique, the thermo-mechanical effect during FSW produces frictional heating and plastic deformation, which contribute to sound joints without defects [10].

So far, no study relevant to the welding of the $(B_4C+Al_2O_3)$/Al composite has been reported to the best of our knowledge. Most studies on the FSW of B_4C/Al composites used 6xxx series alloys as the matrix alloys. For the B_4C/6061Al composites, precipitation state would affect the mechanical properties obviously [12]. Different evolutions of the precipitates such as dissolution and coarsening could lead to softening of the material [13–15]. However, the $(B_4C+Al_2O_3)$/Al composite designed for the long-term application at high temperature is mainly strengthened by Al_2O_3 introduced on the original Al powders, rather than precipitates, thus, different situations may appear in the joints of the $(B_4C+Al_2O_3)$/Al composite. Therefore, more attention should be paid to Al_2O_3 in this composite.

It was considered that the near 3D am-Al_2O_3 netlike structure distributed at the Al grain boundaries (GBs) was the main factor for the high-temperature strengthening [16]. So the high-temperature strength was decreased when this netlike structure was broken in the deformation process or am-Al_2O_3 flakes were transformed into γ-Al_2O_3 particles [16]. Therefore, if the thermo-mechanical effect during FSW would break the netlike structure or result in the Al_2O_3

transformation is worth studying.

In this study, the $(B_4C+Al_2O_3)$/Al composite was friction stir welded and subjected to detailed microstructure characterization and property evaluation. The aims are (1) to study the feasibility of obtaining sound joints by FSW, and (2) to elucidate the influence of the FSW process on the microstructure and mechanical properties of the composite.

2   Experimental procedure

$(B_4C+Al_2O_3)$/Al composite was fabricated by a powder metallurgy (P/M) technique, using Al powders and B_4C particles with mean sizes of 1.45 and 6.5 μm, respectively. Al_2O_3 was formed on the surface of as-atomized Al powders by natural oxidation process. By measuring the oxygen content using LECO TCH600, the mass fraction of Al_2O_3 in Al powders was determined to be 2.3 wt.%. 10 wt.% B_4C particles were mechanically mixed into Al powders in a bi-axis rotary mixer for 8 h. As-mixed powders were cold compacted and then hot pressed into composite billets at 450°C , which is lower than the transformation temperature of am-Al_2O_3 [16]. Then the billets were extruded into plates at 450°C with an extrusion ratio of 9:1. After machining, the $(B_4C+Al_2O_3)$/Al composite plates with a thickness of 12 mm and a width of 90 mm were finally obtained.

The plates were butt-welded along the extrusion direction using a FSW machine. Based on the welding trials, rotation rates of 400, 600 and 800 r/min, and the welding speed of 100 mm/min were selected as the welding parameters, designated as 400–100, 600–100 and 800–100, respectively. The welding tool with a shoulder 24 mm in diameter and a conical threaded pin 12 mm in root diameter was made of ultra-hard cermet, which has been proven to exhibit well wear-resistance when welding 20 wt.% B_4C/Al composites [12].

After welding, the cross-sectional FSW specimens were examined perpendicular to the welding direction by optical microscopy (OM). The OM specimens were mechanically polished and then etched by Keller's reagent. Transmission electron microscopy (TEM, FEI TECNAI F20) observation was carried out to characterize the microstructure of the selected zones of the joints (Figure 1). In this study, the grain size for each zone was counted over 120 grains by TEM examination, and the size of Al_2O_3 was determined by statistical analysis of over 15 TEM images.

The hardness profiles were tested along the mid-thickness line of the cross-sections at an interval of 1 mm, using a Vickers hardness tester (200 g/15 s) (Figure 1). Dog-bone-shaped tensile specimens were machined perpendicular to the welding direction with the nugget zone (NZ) being the center of the gauge. Since tensile specimens with a thickness of 12 mm usually require hydraulic clamps, which are not
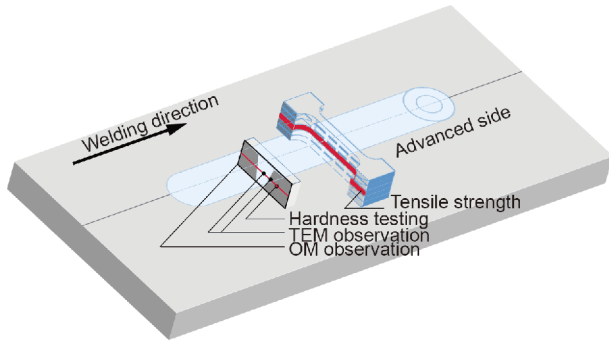
suitable to high-temperature tension, the joints were sliced into thin tensile specimens with a gauge length of 30 mm, a width of 4 mm and a thickness of 2.2 mm (Figure 1). Tensile specimens were tested at a strain rate of 1×10^{-3} s^{-1} at both room temperature (RT) and 375°C (the highest temperature NAMs could experience in the dry storage) using an Instron 5848 tester.

3   Results and discussion

### 3.1   Macroscopic morphologies and macrostructures of the joints

The surfaces of the joints produced at different rotation rates are shown in Figure 2. All the joints exhibited smooth surfaces, with no defect being observed, indicating a good surface quality. A semicircular feature, known as wake effect [10], was observed on the joint surface.

Figure 3 shows the cross-sectional macrostructures of the FSW joints. For each joint, an obvious NZ with a basin shape could be seen. No detectable welding defects were observed in the joints, indicating that sound joints were obtained at all the three rotation rates. Different from most FSW aluminium alloy-based composite joints such as SiC/2009 composite [17], thermo-mechanical affected zone (TMAZ) and heat affected zone (HAZ) could not be identified clearly. It can be ascribed mainly to three reasons. First, the flowability of the composite was suppressed by B_4C and Al_2O_3 particles. Second, Al_2O_3 in the base metal (BM) restricted grain growth, so coarsening of grains in the TMAZ and HAZ was quite slight. Third, it is inherently difficult to form a clear contrast for the pure Al-based PRAMCs by etching.

It can be observed that the width of the NZ increased with increasing the rotation rate. Specifically, the width of the NZs along the central line of the joints was 11.8 mm, 12.1 mm and 13.0 mm for samples 400-100, 600-100 and 800-100, respectively. As pointed out by Mishra and Ma [10], there are mainly two effects of the welding tools: (1) heating the workpiece by the tool/workpiece friction and the
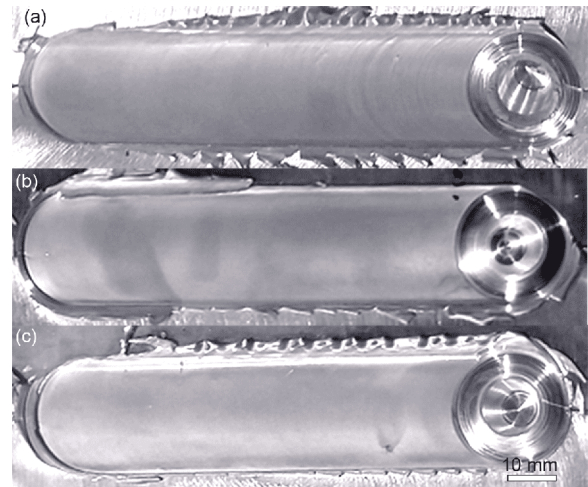
Figure 2   Surface morphologies of (a) sample 400-100, (b) sample 600-100 and (c) sample 800-100.
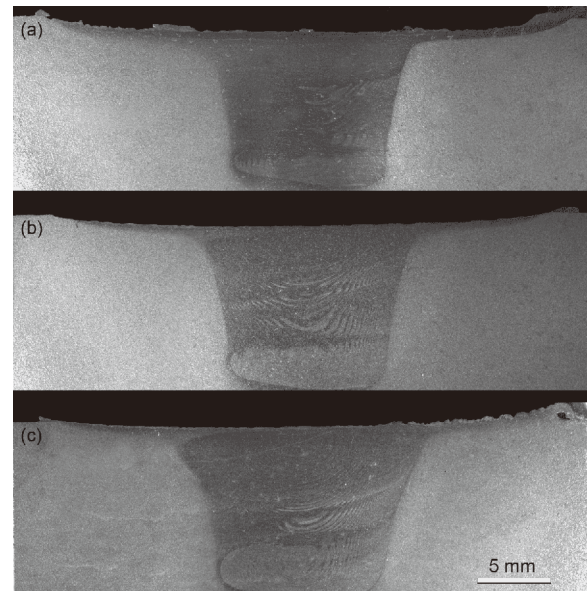

Figure 3   Cross-sectional macrostructures of (a) sample 400-100, (b) sample 600-100 and (c) sample 800-100 (The advancing side is on the right).

material deformation; (2) transporting material. Obviously, with increasing the rotation rate, the welding temperature was higher, and more material was involved in material flow. So, the width of the NZ increased with the rotation rate. Also, with the more sufficient material flow, the onion structure became more integrated.

3.2   Microhardness and mechanical properties

Figure 4 shows the hardness profiles of the transverse cross-section of the FSW joints along the central line. Three characteristics are mainly observed. First, there are apparent three zones: the softened zone around the weld center, the unaffected BM and a transition zone between them. Similar
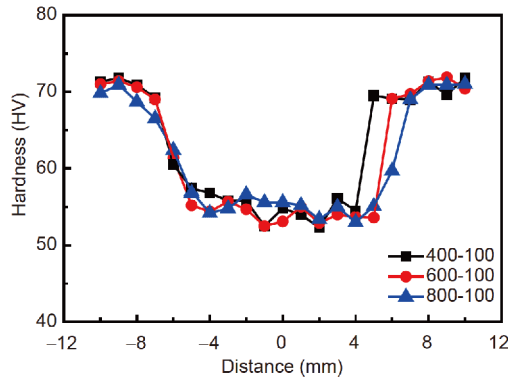
Figure 4 (Color online) Hardness profiles of the transverse section of the FSW joints (The AS is on the right).

situation was also found in the FSW joints of precipitation strengthened Al alloys [18,19] or composites [12]. However, in those studies, the softened zone was quite wider, and the low hardness plateau extended even to the shoulder-affected zone, whereas in the present study, the width of the plateau is only a little bit wider than the pin diameter. The softened zone together with the transition zone was wider than the NZ observed in OM, which indicates that the TMAZ or HAZ were somehow not revealed by OM. Second, with the increase of the rotation rate, the width of low hardness zones was found to increase, but the lowest hardness exhibited almost the same values for the three joints (~ 55 HV), indicating that increasing welding heat input had little influence on the hardness of the NZ. Third, the hardness situation on the advancing side (AS) and retreating side (RS) was

different: the hardness on the AS was slightly lower than that on the RS, and the hardness transition between the NZ and the BM also exhibited different situations. For all samples, the transition of hardness was smooth on the RS. Distinctively, the transition of hardness in samples 400-100 and 600-100 on the AS was sharper, whereas in sample 800-100, a transition zone in hardness existed on the AS at the distance of 5–7 mm away from the weld center, corresponding to the edge of the NZ. The reason will be discussed in Sect. 3.4.

It was found that for each joint, specimens from different layers had the similar tensile properties, so only tensile results of the specimens from the central layer of the joints (Figure 1) were chosen as the representative. Table 1 summarizes the tensile properties at RT and 375°C. Tensile stress-strain curves at RT and 375°C are shown in Figure 5. Compared to the BM, all the joints exhibited decreased tensile strength and elongation at both RT and 375°C. Being consistent with the hardness profile (Figure 4), the strengths of the joints with different rotation rates also exhibited almost the same values, as listed in Table 1.
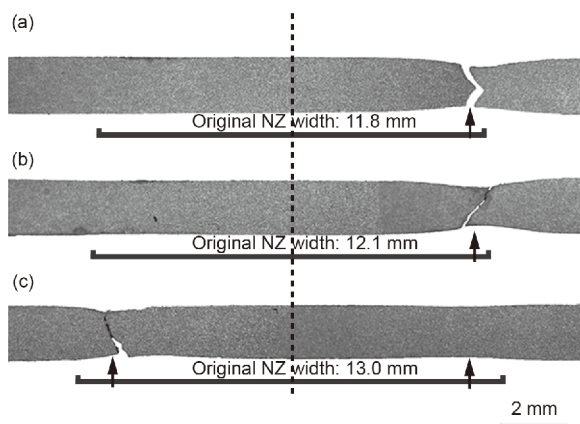
Fractured tensile specimens tested at RT are shown in Figure 6, with the original width of the NZs along the central line of the joints acquired from Figure 3 being labeled. Necking and fracture of all the tensile specimens happened at the edges of the NZs. In previous studies, it was also shown that when a low hardness plateau was formed in a joint, fracture was apt to happen at the edge of the low hardness plateau, most likely because the deformation incompatibility could result in deformation concentration [12,19]. It was also found that fracture of samples 400-100 and 600-100 hap-

Table 1 Tensile properties of the FSW joints and BM at RT and 375°C

Sample	RT			375°C		
	YS (MPa)	UTS (MPa)	El (%)	YS (MPa)	UTS (MPa)	El (%)
BM	190.1	223.0	12.9	100.3	105.6	6.3
400-100	132.1	173.2	6.7	71.1	72.7	2.3
600-100	131.7	171.5	7.5	71.0	72.0	2.8
800-100	135.1	173.6	9.2	70.0	71.9	3.2
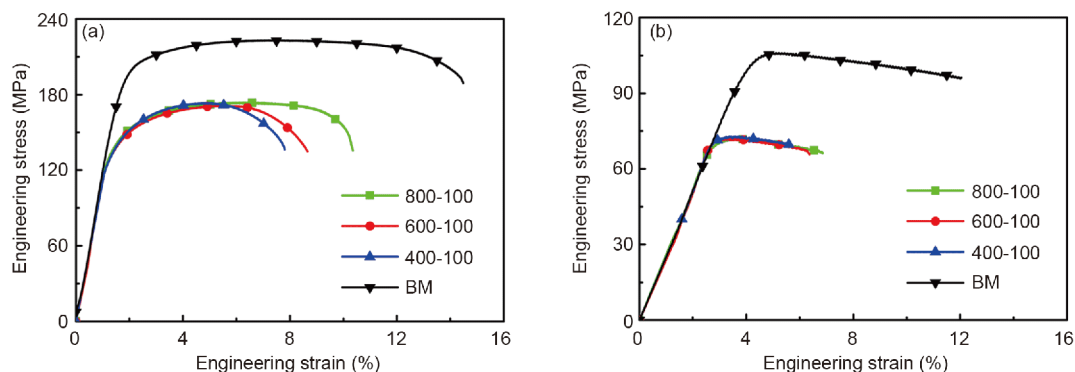
Figure 5 (Color online) Tensile stress-strain curves of the FSW joints under different welding parameters at (a) RT and (b) 375°C.

Figure 6 Fractured tensile specimens of (a) sample 400-100, (b) sample 600-100 and (c) sample 800-100 tested at RT (The advancing side is on the right).
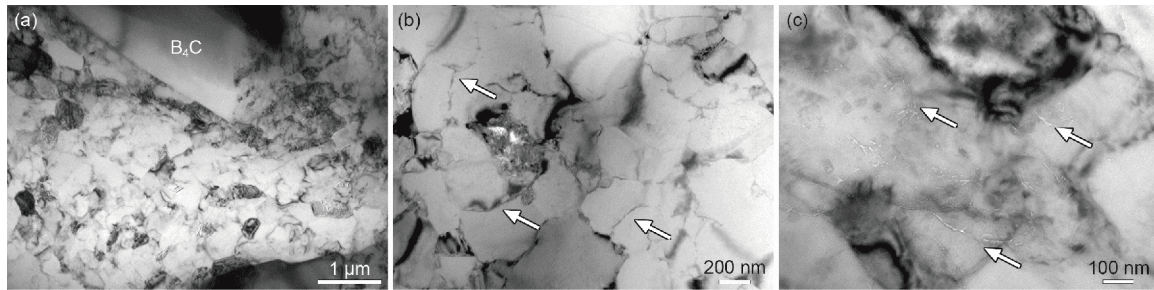

Figure 7 Optical micrographs showing the distribution of B_4C particles in (a) BM and NZs of sample 400-100 (b), sample 600-100 (c) and sample 800-100 (d).

pened on the AS, but when rotation rate increased to 800 r/min, fracture happened on the AS or the RS randomly. This is easily understood for samples 400-100 and 600-100, because the NZ edge on the AS exhibited the lowest hardness, and the sudden change in hardness on the AS would further prompt deformation concentration and fracture. When the rotation rate increased to 800 r/min, the hardness of the NZ edge on the AS and the RS became closer, and a hardness transition zone appearing at the NZ edge on the AS reduced the fracture tendency in this region. As shown in Figure 6, necking in sample 800-100 happened at the NZ edges of both the AS and the RS (as denoted by arrows), thus the fracture location became more random for sample 800-100. Fracture behaviour at 375°C exhibited the same situation as it did at RT.

3.3 Microstructure evolution of the joints

By observation of macroscopic morphologies and macrostructures of the joints, all the joints were free of welding defects, so it is necessary to further investigate the microstructure of the joints to disclose the reason for strength degeneration. Figure 7 shows the microstructure of the BM (Figure 7(a)) and NZs in samples 400-100 (Figure 7(b)), 600-100 (Figure 7(c)) and 800-100 (Figure 7(d)). Compared to that in the BM, the distribution of B_4C particles in the NZs was more homogeneous due to the deformation in the FSW process. Also, the cusps of B_4C particles were blunted to some extent in the NZs, especially for sample 800-100.

Figure 8 shows the TEM images of the $(B_4C+Al_2O_3)/Al$ composite. An ultrafine structure could be seen in the BM, with an average grain size of about 276 nm (Figure 8(a)). Furthermore, a clean interface between B_4C particles and Al matrix was observed, indicating no obvious interfacial reaction, which can be attributed to the low hot-pressing temperature. Under a higher magnification, a near 3D netlike
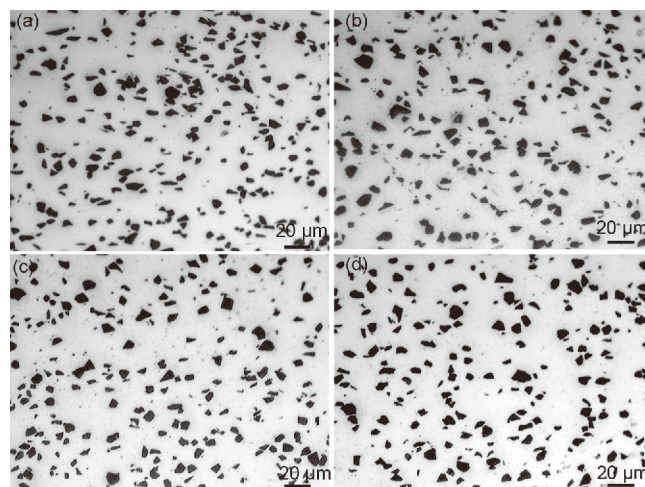
Al_2O_3 structure with the lamellar Al_2O_3 being distributed in the Al grain boundaries could be seen (Figure 8(b)). As reported in refs. [16,20], the lamellar shape of Al_2O_3 corresponds to the characteristic of am-Al_2O_3. It was because the hot-pressing temperature used in this study was lower than the crystallization temperature of am-Al_2O_3. The lamellar am-Al_2O_3 was distributed mostly at the GBs, being consistent with the study of as-extruded Al_2O_3/Al composite compacted with ultrafine Al powders [16]. Figure 8(c) shows am-Al_2O_3 distribution parallel to the extrusion direction. The average length of Al_2O_3 along the extrusion direction was determined as 105 nm.

Figure 9 shows the grain microstructure of the NZs in the FSW joints. It was shown that the near 3D netlike structure was totally broken. Compared with that in the BM, the size of the grains in the NZs increased substantially and a coarse-grained structure took the place of the ultrafine-grained structure. Grains with an average size of 960 nm could be observed clearly, which were obviously coarser than those in the BM (Figure 8).

Generally speaking, higher rotation rate can generate more heat, resulting in higher welding temperature and consequently coarser grains [21]. However, in this study, no significant difference in the grain size was observed in the joints obtained at different rotation rates. It is possibly because that the grain growth in the composite was restricted by the Al_2O_3 particles due to their significant GB pinning effect. Therefore, the grain size of the NZs of the FSW joints was mostly decided by the interspacing of Al_2O_3, and the influence of the FSW parameters was inconspicuous.

The characterization of the Al_2O_3 distribution in the NZ of sample 800-100 is shown in Figure 10. Figure 10(a) and (b) shows the same field of view using two different observation tilt angles, in order to disclose the GBs and Al_2O_3 clearly. It

Figure 8 TEM micrographs showing (a) microstructure of (B$_4$C+Al$_2$O$_3$)/Al composite, and am-Al$_2$O$_3$ (b) perpendicular and (c) parallel to the extrusion direction in the composite under a higher magnification (white arrows indicated the distribution of am-Al$_2$O$_3$).
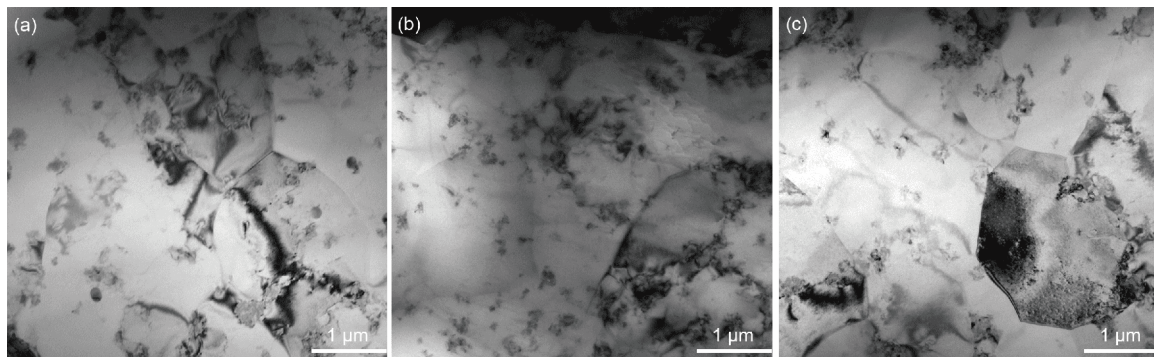
Figure 9 TEM micrographs showing the microstructure of the NZs in (a) sample 400-100, (b) sample 600-100 and (c) sample 800-100.
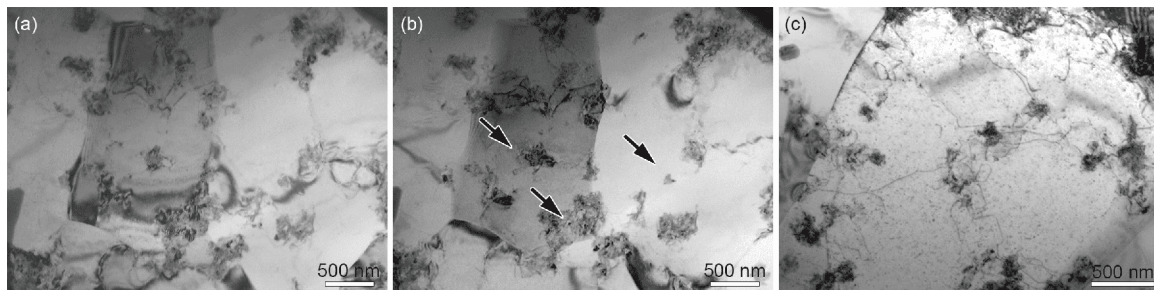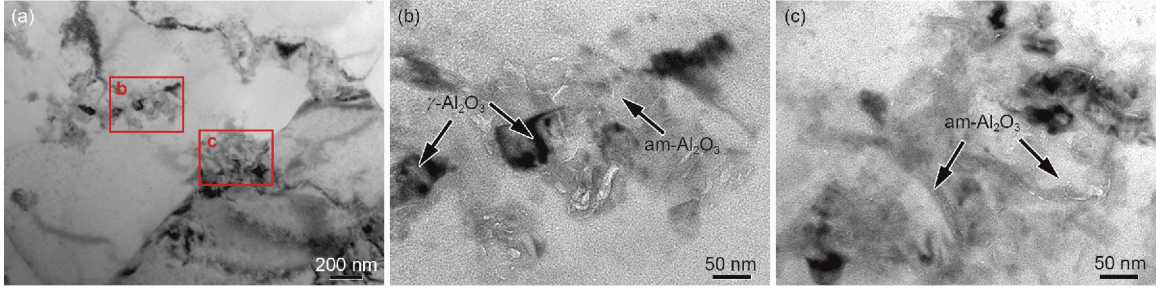

Figure 10 TEM micrographs showing Al$_2$O$_3$ distribution in the NZ of sample 800-100. (a) and (b) The same field of view with different observing tilts and (c) Al$_2$O$_3$ tangled with the dislocations.

was found that the Al$_2$O$_3$ (indicated by arrows) was distributed at the GBs, sub-GBs or in the interior of the grains. Furthermore, the Al$_2$O$_3$ no longer exhibited the lamellar morphology as they did in the BM, and a clustering behavior was observed instead. The average size of Al$_2$O$_3$ clusters was determined as 225 nm by statistical analysis. In Figure 10(c), it could be also seen that Al$_2$O$_3$ in the grain interior was tangled with the dislocations. From these observations, it can be concluded that the original near 3D netlike microstructure was destroyed in the FSW process.

From Figure 11, it can be seen that clusters of Al$_2$O$_3$ were composed of both am-Al$_2$O$_3$ and γ-Al$_2$O$_3$. The magnifications of the selected areas in Figure 11(a) (red frames) are shown in Figure 11(b) and (c). The am-Al$_2$O$_3$ film exhibited a wrinkled morphology, as the result of the thermo-mechanical effect of the welding pin. Moreover, a few particles

with a diameter of about 50 nm was found, which was consistent with the characteristic of γ-Al$_2$O$_3$ [16]. It is considered that part of am-Al$_2$O$_3$ was transformed into γ-Al$_2$O$_3$ under the thermo-mechanical effect during FSW.

Figure 12 shows TEM images of a specimen taken from the edge of the NZ on the AS (as shown in Figure 1) of sample 800-100, which corresponds to the hardness transition zone. As shown in Figure 12(a), the grain structure was found to experience less deformation compared to the NZ and elongated grain structure was observed. Material deformation and flow in this zone were caused by adjacent material instead of the direct stirring effect of the pin, so the grain structure experienced little change compared to the NZs and elongated grains with an average thickness of 520 nm were observed. The elongated characteristic of the grains conformed to the microstructural characteristics of the

Figure 11 (Color online) TEM micrographs showing Al_2O_3 in the NZ of sample 800-100. (b) and (c) are magnified views of selected regions in (a).
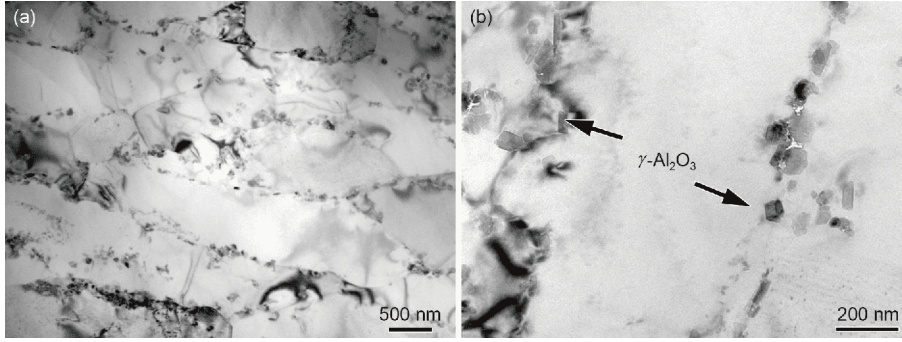
Figure 12 TEM micrographs revealing (a) the grain structure and (b) Al_2O_3 in the TMAZ of sample 800-100 on the AS.

TMAZ, so the existence of the TMAZ in sample 800-100 was confirmed. At higher magnification, it was seen that original lamellar structure of am-Al_2O_3 was broken and some γ-Al_2O_3 particles were also found in this zone, i.e., the TMAZ (Figure 12(b)).

3.4 Reasons for mechanical property variation

By summarizing strengthening mechanisms, the yield strength of the composites at RT can be expressed as [22]

$$\sigma_{yc}=\sigma_{ym}+\sigma_{Al_2O_3}+\sigma_{B_4C}, \qquad (1)$$

where σ_{yc} is the yield strength of the composite, σ_{ym} the yield strength of Al matrix, $\sigma_{Al_2O_3}$ the strengthening effect of Al_2O_3, and σ_{B_4C} the strengthening effect of B_4C.

σ_{ym} can be estimated by [23]

$$\sigma_{ym}=\sigma_0+\sigma_{H\text{-}P}, \qquad (2)$$

where σ_0 is a friction stress and $\sigma_{H\text{-}P}$ is the Hall-Petch strengthening of matrix. According to the Hell-Petch relation for Al [23,24], the σ_{ym} of the BM and the NZ can be estimated as 127 and 69 MPa, respectively.

$\sigma_{Al_2O_3}$ can be expressed as

$$\sigma_{Al_2O_3} = \sigma_{Al_2O_3}^{\text{L-T}} + \sigma_{Al_2O_3}^{\text{GND}} + \sigma_{Al_2O_3}^{\text{Oro}}, \qquad (3)$$

where $\sigma_{Al_2O_3}^{\text{L-T}}$ is the result of load-transfer strengthening, $\sigma_{Al_2O_3}^{\text{Oro}}$ the strength increase caused by Orowan strengthening, and $\sigma_{Al_2O_3}^{\text{GND}}$ the strength increase caused by geometrically

necessary dislocations (GNDs) formed in the tensile process due to mismatch in elastic modulus.

For lamellar Al_2O_3 in the BM, $\sigma_{Al_2O_3}^{\text{L-T}}$ can be calculated as [22]

$$\sigma_{Al_2O_3}^{\text{L-T}}=\frac{L\sigma_{ym}}{4t}V_P, \qquad (4)$$

where L is the length of Al_2O_3 along the tensile direction, t the thickness of Al_2O_3, and V_P the volume fraction of Al_2O_3. According to our previous study [25], t is 5 nm and V_P is 2.1 vol.%. So $\sigma_{Al_2O_3}^{\text{L-T}}$ in the BM is calculated as 14 MPa.

However, when calculating $\sigma_{Al_2O_3}^{\text{L-T}}$ in the NZ, because the lamellar shape was destroyed in the FSW process (as shown in Figure 9), and Al_2O_3 was clustered as equiaxed morphology, the following equation for calculating load-transfer strengthening effect of particulate reinforcements should be used [26]:

$$\sigma_{Al_2O_3}^{\text{L-T}}=0.5V_P\sigma_{ym}, \qquad (5)$$

according to which, $\sigma_{Al_2O_3}^{\text{L-T}}$ in the NZ can be calculated as 1 MPa.

$\sigma_{Al_2O_3}^{\text{GND}}$ in the BM and the NZ can be calculated as [27]

$$\sigma_{GND}=\alpha Gb\sqrt{\frac{8V_P\varepsilon_y}{bD}}, \qquad (6)$$

where α is a constant (1.25), G the shear modulus of Al (26.4 GPa), b the Burgers vector (0.286 nm), D approximately the average diameter of the particles, and ε_y the yielding strain

(0.2%). According to this formula, $\sigma_{\text{Al}_2\text{O}_3}^{\text{GND}}$ in the BM and the NZ was 32 and 22 MPa, respectively.

Since Al_2O_3 in the BM was predominantly distributed at the GBs, they could not effectively contribute to strengthening by Orowan mechanism [16]. Therefore, $\sigma_{\text{Al}_2\text{O}_3}^{\text{Oro}}$ in the BM can be neglected. However, in the NZ, a large portion of Al_2O_3 entered in the Al grains, thus, $\sigma_{\text{Al}_2\text{O}_3}^{\text{Oro}}$ should be considered, which can be expressed as [28]

$$\sigma_{\text{Oro}} = \frac{0.13Gb}{D\left[\left(\dfrac{1}{2V_P}\right)^{\frac{1}{3}} - 1\right]} \ln\frac{D}{2b}. \tag{7}$$

Thus, $\sigma_{\text{Al}_2\text{O}_3}^{\text{Oro}}$ in the NZ was 15 MPa.

$\sigma_{\text{B}_4\text{C}}$ can be expressed as

$$\sigma_{\text{B}_4\text{C}} = \sigma_{\text{B}_4\text{C}}^{\text{L-T}} + \sigma_{\text{B}_4\text{C}}^{\text{GND}}, \tag{8}$$

where $\sigma_{\text{B}_4\text{C}}^{\text{L-T}}$ can be calculated by eq. (5), and $\sigma_{\text{B}_4\text{C}}^{\text{GND}}$ can be calculated by eq. (6). The values of $\sigma_{\text{B}_4\text{C}}^{\text{L-T}}$ in the BM and the NZ were 7 and 4 MPa, respectively, and values of $\sigma_{\text{B}_4\text{C}}^{\text{GND}}$ in the BM and the NZ were both 9 MPa.

According to eqs. (1), (3), and (8), σ_{yc} of the BM and the NZ was calculated as 189 and 120 MPa. By comparison with Table 1, it can be seen the calculated values of yield strength are quite close to the experimental yield strength. Lower calculated yield strength of the NZ may be because some Al_2O_3 still remain lamellar shape, contributing to higher $\sigma_{\text{Al}_2\text{O}_3}^{\text{L-T}}$ and $\sigma_{\text{Al}_2\text{O}_3}^{\text{Oro}}$.

Based on the microstructure characterization and strength analysis, it can be proposed that the drop in hardness of the NZs and strength degeneration of the FSW joints at RT can be mainly ascribed to the following two reasons: (1) weakening of fine-grain strengthening due to the coarser grains; (2) weakening of strengthening effect of the Al_2O_3 because of the breakup of the uniformly distributed lamellar am-Al_2O_3 in the FSW process.

Moreover, the transition situation in microhardness between the NZ and the BM as well as the fracture behavior of the joints can be well explained. Under low heat input, the original material on the AS was taken away directly when it contacted with the pin and then replaced by material experiencing more sufficient deformation; by comparison, the material deformation on the RS was less sufficient [29,30]. Therefore, the transition of hardness was smoother on the RS.

With increasing the rotation rate to 800 r/min, the higher welding heat input could result in a wider softened region, so sufficient flow was caused by the thermo-mechanical effect. In the TMAZ, deformation was not driven by the stirring pin

directly but by adjacent material flow. The grain structure in the TMAZ was finer than that in the NZ (as shown in Figures 9 and 12), and the hardness in the TMAZ was higher than that in the NZ as a result. Therefore, the hardness transition became smoother at high rotation rate of 800 r/min in the TMAZ on the AS, which further resulted in the variation of the fracture location.

At 375°C, the stability of the GBs became more important [31], therefore, the GB stabilization effect of lamellar Al_2O_3 with the netlike distribution was of prime importance. It was reported that reinforcements with a 3D netlike distribution in the Al matrix could improve high-temperature strength to a large extent [32]. Therefore, with the breakdown of the netlike structure, the strengthening effect became much weaker. The joint efficiency at 375°C (about 69%) was lower than that at RT (about 77%). Clearly, the strengthening effect of lamellar Al_2O_3 with the netlike distribution was more important for high-temperature strength.

The deformation during the tensile process was concentrated in the NZ, so the joints exhibited lower elongation at RT and 375°C compared with the BM. With the increase of rotation rate, the NZs became wider, thus the elongation of the joints increased.

The overall implication of the experimental results obtained in this study is significant. It was proven that the thermo-mechanical effect in the FSW process resulted in the breakup of the 3D netlike distribution of Al_2O_3, thereby degrading the mechanical properties of the joints. However, it was found that changing rotation rate cannot increase the strength. The future study will be focused on improving the strength of the joints through decreasing heat input by higher welding speed or submerged FSW.

4   Conclusions

(1) Sound joints of $(\text{B}_4\text{C}+\text{Al}_2\text{O}_3)/\text{Al}$ composites were obtained with rotation rates of 400, 600, and 800 r/min at a constant welding speed of 100 mm/min. No welding defects were detected in the joints.

(2) Hardness of the nugget zones (NZs) was lower than that of the base metal (BM) and tensile strength of the joints decreased as a result. The joints with different rotation rates exhibited similar strength, and joint efficiencies of about 77% and 69% were obtained at RT and 375°C, respectively, with the joints fracturing in the edge of the NZs.

(3) After FSW, a coarse-grained structure took the place of the ultrafine-grained structure of the BM. The original structure with a near netlike lamellar am-Al_2O_3 being distributed at the Al GBs was destroyed. Al_2O_3 was aggregated and partially crystallized into γ-Al_2O_3.

(4) The weakening of fine-grain strengthening and load-transfer strengthening of Al_2O_3 caused the strength decrease

at room temperature, and the breakdown of netlike distribution of Al_2O_3 resulted in severe strength decline at 375°C.

1   Li Y, Wang W, Zhou J, et al. 10 B areal density: A novel approach for design and fabrication of B_4C/6061Al neutron absorbing materials. J Nucl Mater, 2017, 487: 238–246

2   Chen H S, Wang W X, Li Y L, et al. The design, microstructure and mechanical properties of B_4C/6061Al neutron absorber composites fabricated by SPS. Mater Des, 2016, 94: 360–367

3   Tariq N H, Gyansah L, Qiu X, et al. Achieving strength-ductility synergy in cold spray additively manufactured Al/B_4C composites through a hybrid post-deposition treatment. J Mater Sci Tech, 2019, 35: 1053–1063

4   Chen H S, Wang W X, Nie H H, et al. Microstructure evolution and mechanical properties of B_4C/6061Al neutron absorber composite sheets fabricated by powder metallurgy. J Alloys Compd, 2018, 730: 342–351

5   Zan Y N, Zhang Q, Zhou Y T, et al. Enhancing high-temperature strength of B_4C–6061Al neutron absorber material by in-situ Mg(Al) B_2. J Nucl Mater, 2019, 526: 151788

6   Xu Z G, Jiang L T, Zhang Q, et al. The formation, evolution and influence of Gd-Containing phases in the (Gd+B_4C)/6061Al composites during hot rolling. J Alloys Compd, 2019, 775: 714–725

7   Zan Y N, Zhou Y T, Liu Z Y, et al. Enhancing strength and ductility synergy through heterogeneous structure design in nanoscale Al_2O_3 particulate reinforced Al composites. Mater Des, 2019, 166: 107629

8   Ureña A, Escalera M D, Gil L. Influence of interface reactions on fracture mechanisms in TIG arc-welded aluminium matrix composites. Compos Sci Tech, 2000, 60: 613–622

9   Ellis M B D. Joining of al-based metal matrix composites - A review. Mater Manufacturing Processes, 1996, 11: 45–66

10   Mishra R S, Ma Z Y. Friction stir welding and processing. Mater Sci Eng-R-Rep, 2005, 50: 1–78

11   Moradi M M, Jamshidi Aval H, Jamaati R, et al. Effect of SiC nanoparticles on the microstructure and texture of friction stir welded AA2024/AA6061. Mater Charact, 2019, 152: 169–179

12   Li Y Z, Zan Y N, Wang Q Z, et al. Effect of welding speed and post-weld aging on the microstructure and mechanical properties of friction stir welded B_4C_p/6061Al-T6 composites. J Mater Processing Tech, 2019, 273: 116242

13   Chen X G, da Silva M, Gougeon P, et al. Microstructure and mechanical properties of friction stir welded AA6063-B_4C metal matrix composites. Mater Sci Eng-A, 2009, 518: 174–184

14   Chen H S, Wang W X, Nie H H, et al. Nanoindentation and tensile properties of FSW Joints of B_4C/6061Al neutron absorbers. Rare Metal Mat Eng, 2017, 46: 392–398

15   Tao X, Chang Y, Guo Y, et al. Microstructure and mechanical properties of friction stir welded oxide dispersion strengthened AA6063 aluminum matrix composites enhanced by post-weld heat treatment. Mater Sci Eng-A, 2018, 725: 19–27

16   Balog M, Poletti C, Simancik F, et al. The effect of native Al_2O_3 skin disruption on properties of fine Al powder compacts. J Alloys Compd, 2011, 509: S235–S238

17   Feng A, Xiao B, Ma Z. Effect of microstructural evolution on mechanical properties of friction stir welded AA2009/SiC_p composite. Compos Sci Tech, 2008, 68: 2141–2148

18   Zhao H, Pan Q, Qin Q, et al. Effect of the processing parameters of friction stir processing on the microstructure and mechanical properties of 6063 aluminum alloy. Mater Sci Eng-A, 2019, 751: 70–79

19   Peel M, Steuwer A, Preuss M, et al. Microstructure, mechanical properties and residual stresses as a function of welding speed in aluminium AA5083 friction stir welds. Acta Mater, 2003, 51: 4791–4801

20   Balog M, Hu T, Krizik P, et al. On the thermal stability of ultrafine-grained Al stabilized by in-situ amorphous Al_2O_3 network. Mater Sci Eng-A, 2015, 648: 61–71

21   Nandan R, Debroy T, Bhadeshia H. Recent advances in friction-stir welding-process, weldment structure and properties. Prog Mater Sci, 2008, 53: 980–1023

22   Zan Y N, Zhou Y T, Zhao H, et al. Enhancing high-temperature strength of (B_4C+Al_2O_3)/Al designed for neutron absorbing materials by constructing lamellar structure. Compos Part B-Eng, 2020, 183: 107674

23   Kai X Z, Li Z Q, Fan G L, et al. Enhanced strength and ductility in particulate-reinforced aluminum matrix composites fabricated by flake powder metallurgy. Mater Sci Eng-A, 2013, 587: 46–53

24   Maung K, Earthman J C, Mohamed F A. Inverse Hall–Petch behavior in diamantane stabilized bulk nanocrystalline aluminum. Acta Mater, 2012, 60: 5850–5857

25   Zan Y N, Zhou Y T, Liu Z Y, et al. Microstructure and mechanical properties of (B_4C+Al_2O_3)/Al composites designed for neutron absorbing materials with both structural and functional usages. Mater Sci Eng-A, 2019, 138840

26   Ramakrishnan N. An analytical study on strengthening of particulate reinforced metal matrix composites. Acta Mater, 1996, 44: 69–77

27   Tang F, Anderson I E, Gnaupel-Herold T, et al. Pure Al matrix composites produced by vacuum hot pressing: tensile properties and strengthening mechanisms. Mater Sci Eng-A, 2004, 383: 362–373

28   Zhang Z, Topping T, Li Y, et al. Mechanical behavior of ultrafine-grained Al composites reinforced with B_4C nanoparticles. Scripta Mater, 2011, 65: 652–655

29   Chen G, Li H, Wang G, et al. Effects of pin thread on the in-process material flow behavior during friction stir welding: A computational fluid dynamics study. Int J Machine Tools Manufacture, 2018, 124: 12–21

30   Xu S. A study of texture patterns in friction stir welds. Acta Mater, 2008, 56: 1326–1341

31   Poletti C, Balog M, Simancik F, et al. High-temperature strength of compacted sub-micrometer aluminium powder. Acta Mater, 2010, 58: 3781–3789

32   Hu K, Xu Q, Ma X, et al. A novel heat-resistant Al-Si-Cu-Ni-Mg base material synergistically strengthened by Ni-rich intermetallics and nano-AlN_p microskeletons. J Mater Sci Tech, 2019, 35: 306–312